

C 7 Lorentz microscopy and electron holography of skyrmions

András Kovács and Rafal E. Dunin-Borkowski

Ernst Ruska-Centre for Microscopy and Spectroscopy with
Electrons and Peter Grünberg Institut

Forschungszentrum Jülich GmbH

Contents

1	Introduction	2
2	Magnetic imaging in the transmission electron microscope	3
2.1	Fresnel imaging	4
2.2	Off-axis electron holography	7
3	Quantitative measurements of skyrmions in <i>B20</i>-type FeGe	13
3.1	Temperature and magnetic field dependence	13
3.2	<i>In situ</i> magnetization switching of a skyrmion lattice	15
3.3	Skyrmions in confined geometries	18
3.4	Magnetization and hexagonal distortion of skyrmions	21
4	Summary	21

1 Introduction

Magnetic skyrmions are nanoscale spin objects that are usually stabilised in chiral magnets and bilayer thin films due to the Dzyaloshinskii-Moriya interaction (DMI). The existence of stable magnetic skyrmions in chiral magnetic materials was predicted theoretically by Bogdanov and Yablonskii in 1989 [1]. However, experimental proof of the phenomenon was not available until 2009, when the A-phase in a bulk *B20*-type Mn-Si single crystal was observed using neutron diffraction [2]. Intense interest in these materials arose after breakthrough results showing the direct real space observation of magnetic skyrmions in an Fe-Co-Si thin film using Lorentz transmission electron microscopy (LTEM) [3]. The ability to move magnetic skyrmions in lateral directions using extremely low electrical currents [4] triggered interest in their use in new magnetic data storage and spintronics technologies, in which the skyrmions act as data bit carriers and can be moved along a ferromagnetic stripe that takes on the role of a guiding track. The real space observation of skyrmions with high spatial resolution is essential to study their basic geometrical parameters, magnetic structure, movement, creation and deformation in the presence of external stimuli such as magnetic field, temperature, mechanical strain and electrical current.

Transmission electron microscopy (TEM) is generally used to obtain quantitative measurements of the structural, electronic and chemical properties of materials on length scales down to the sub-ngstrom level. In the last decade, electron microscopy has been revolutionized by the introduction of aberration correctors, high brightness electron guns, monochromators and advanced detectors, as well as by improvements in computing power for microscope control, image processing and image simulation. However, TEM also has a strong track record in providing real space quantitative magnetic information about materials with nm spatial resolution. A photograph of a modern aberration corrected TEM that is capable of both atomic resolution structural imaging and recording high spatial resolution magnetic information about materials is shown in Fig. 1. Magnetic imaging in the TEM is based on the interaction of incident high energy electrons with the magnetic field within and around a sample. Here, we concentrate on the use of two complementary phase contrast techniques in the TEM, Fresnel imaging and off-axis electron holography, to record magnetic information from electron-transparent samples that contain magnetic skyrmions.

Magnetic skyrmions possess topological stability. The topological invariant

$$n_{skyrm} = \frac{1}{4\pi} \int \hat{n} \cdot (\partial_x \hat{n} \times \partial_y \hat{n}) dx dy, \quad (1)$$

where \hat{n} is the normalized spin direction, is often called the skyrmion number or winding number and describes the number of times that a spin vector wraps the entire sphere. A single skyrmion has a topological number of 1 (or -1), which cannot be changed by a continuous deformation. However, the fact that this number is fixed allows various magnetic configurations, as shown in Fig. 2. In a Bloch-type skyrmion (or vortex), the spins rotate in the tangential plane, *i.e.*, perpendicular to the radial direction when moving from the core to the periphery. In a Neel-type skyrmion (or hedgehog), the spins rotate in the radial plane from the core to the periphery. It is worth noting that the skyrmion structure is topologically equivalent to that of a magnetic bubble [5]. A magnetic bubble is a magnetic structure that is characterised by a core domain region, in which the magnetic moment is normal to the surface plane, a peripheral region in which the magnetic moment is antiparallel to the core and a circular domain wall region that connects the core to the periphery with a continuous magnetic moment distribution, as shown

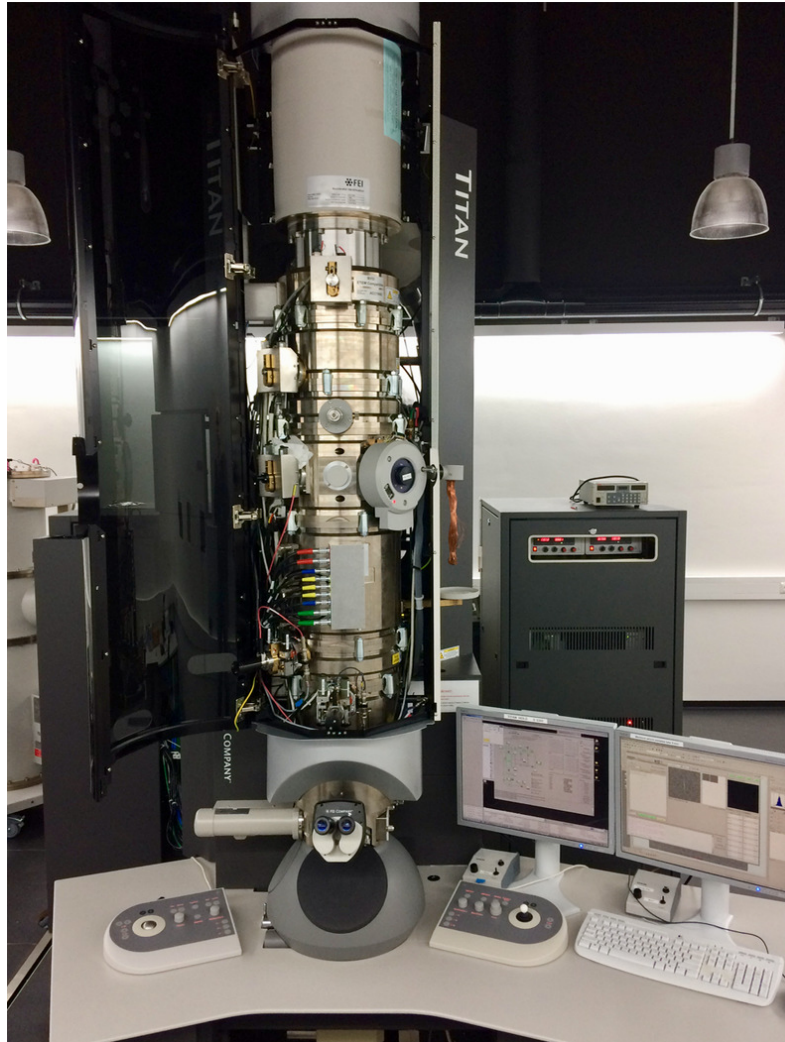


Fig. 1: FEI Titan 80-300 field emission gun transmission electron microscope in the Ernst-Ruska Centre for Microscopy and Spectroscopy with Electrons in Forschungszentrum Jülich. The microscope is equipped with a high brightness electron gun, an image aberration corrector, an 11 mm objective lens polepiece gap, a non-immersion Lorentz lens, two electrostatic biprisms separated by an extra lens and a post-column imaging spectrometer.

in Fig. 2(c). Magnetic bubble domains can form in thin films with strong anisotropy. In this chapter, we focus on Bloch-type magnetic skyrmions in $B20$ -type chiral magnets and on the measurement of their magnetic properties in the TEM.

2 Magnetic imaging in the transmission electron microscope

In the TEM, a highly accelerated electron beam passes through an electron-transparent solid (or liquid or gas) sample, providing access to its structural and chemical properties with atomic spatial resolution. In conventional TEM, a thin (usually below 100-nm-thick) specimen is irradiated with an electron beam that has been accelerated by 60-300 kV. The incident electrons interact strongly with the atomic columns in the sample through elastic and inelastic scattering, resulting in a variety of signals that are characteristic of the sample and can be recorded

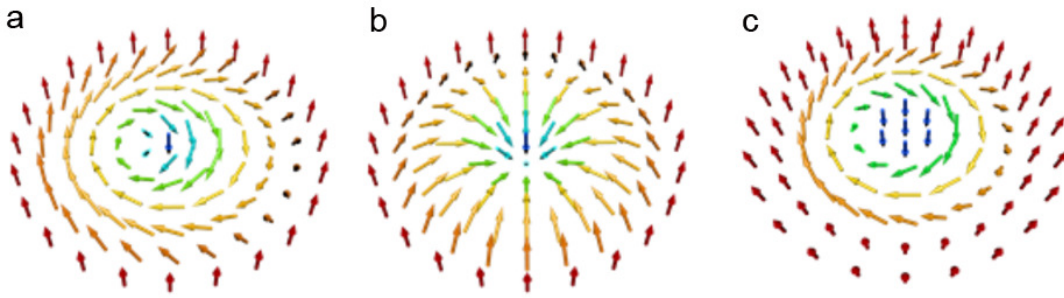


Fig. 2: Spin configurations of (a) a Bloch-type skyrmion, (b) a Néel-type skyrmion and (c) a magnetic bubble.

using imaging, diffraction or spectroscopy [6]. The electrons are emitted from an electron gun and focused onto the sample using a condenser lens system in a high vacuum electron column. An objective lens is used to form images or diffraction patterns of the sample, which are then magnified using projector lenses onto a detector, such as a charge-coupled device (CCD) camera. The electromagnetic lenses in the microscope column suffer from aberrations. The main resolution-limiting aberration is the spherical aberration of the objective lens, which introduces an additional scattering-angle-dependent phase shift to electrons that have interacted with the sample. The spherical aberration coefficient C_s of a conventional electron microscope objective lens is approximately 1 mm. However, recent developments in hardware aberration correctors for electron microscopes now allow C_s to be tuned, providing sub-Å spatial resolution and picometer precision in the measurements of atomic column positions, even in three dimensions [7].

The magnetic field of the conventional objective lens in a TEM is usually in the range of 2 T, which fully saturates most magnetic materials in the electron beam direction during TEM studies. A key requirement for studying the magnetic properties of materials using phase contrast techniques in the TEM is to place them in a magnetic-field-free environment. This situation can usually be achieved by turning off the conventional microscope objective lens and using, instead, either a dedicated Lorentz mini-lens or the transfer lens of an aberration corrector unit. As these lenses are located far from the sample, the electron-optical performance of the microscope is then decreased. The use of a spherical aberration corrector can then be used to reduce the C_s value of a Lorentz lens from several metres to below 1 mm, thereby providing improved spatial resolution. Several of the imaging modes that are available in magnetic-field-free conditions in the TEM are referred to broadly as “Lorentz microscopy”. In this chapter, the Fresnel mode of Lorentz microscopy and the technique of off-axis electron holography are introduced and their application to the study of the magnetic properties of Bloch-type magnetic skyrmions is described. Figure 3 shows simplified ray diagrams for the two techniques when they are implemented in a TEM that is equipped with a Lorentz lens and an aberration corrector.

2.1 Fresnel imaging

In the presence of an electric field \mathbf{E} and a magnetic field \mathbf{B} , electrons in a TEM experience the Lorentz force

$$\mathbf{F} = -e(\mathbf{E} + v \times \mathbf{B}), \quad (2)$$

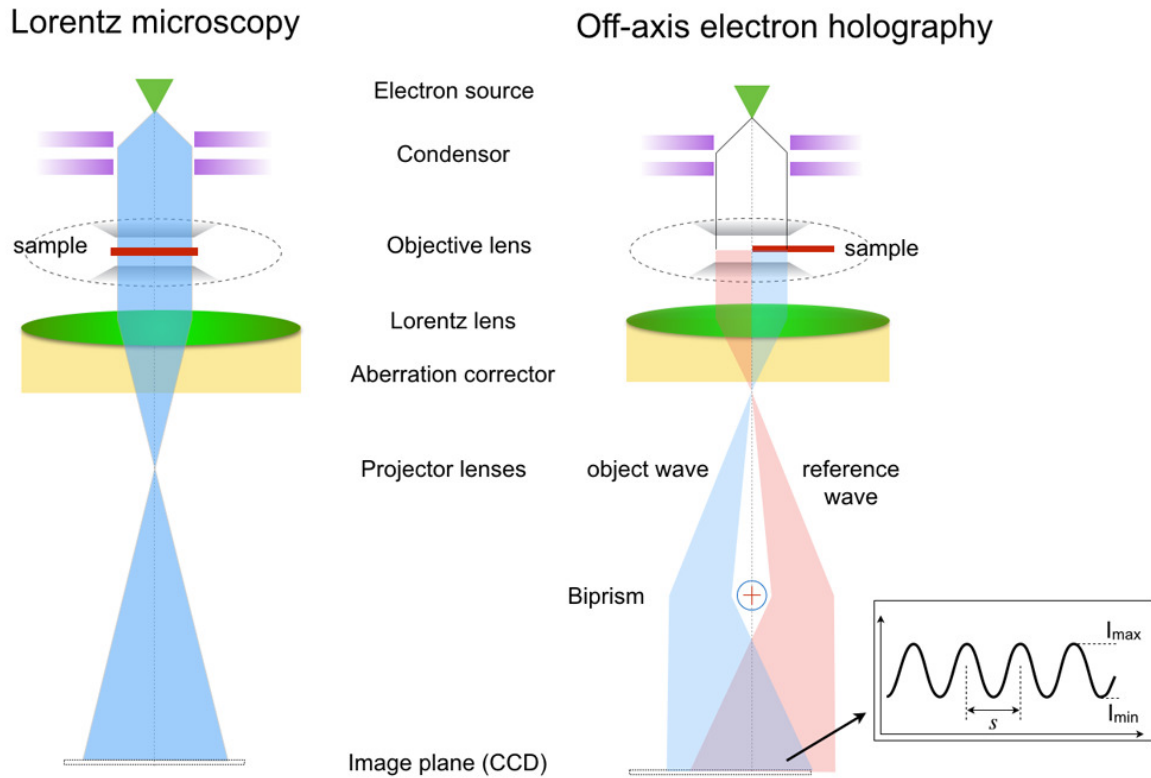


Fig. 3: Simplified schematic ray diagrams for Lorentz microscopy and off-axis electron holography in the transmission electron microscope. For each technique, the conventional microscope objective lens is switched off in order to create a magnetic-field-free environment at the position of the sample. In off-axis electron holography, the interference pattern is characterized by fringe spacing s and fringe contrast C . The latter parameter is determined from the maximum and minimum interference fringe intensities I_{max} and I_{min} measured in vacuum.

where e is the magnitude of the electron charge and v is the velocity of the incident electrons. The force generated by the magnetic part of Eq. (2) is perpendicular to the electron velocity and to the direction of the magnetic field. To a first approximation, the presence of an in-plane magnetic field B_{\perp} in a TEM sample of thickness t results in the small-angle deflection of an incident electron by an angle

$$\vartheta = \frac{e\lambda}{h} B_{\perp} t, \quad (3)$$

where λ is the (relativistic) wavelength of the electrons and h is Planck's constant. For electrons that have been accelerated by 300 kV and pass through a specimen of thickness 100 nm that supports an in-plane magnetic induction of 1 T, the deflection angle is 47.6 μ rad. For comparison, typical crystallographic Bragg angles in electron diffraction in the TEM are in the range of a few *milliradians*, *i.e.*, much larger than Lorentz deflection angles. The deflection of the electrons can be exploited to image the magnetic structure of a thin film by recording defocused images (Fresnel mode) or by selecting only those electrons that have been deflected in a specific direction using either an aperture (Foucault mode) or a segmented detector (differential phase contrast (DPC) imaging in the scanning TEM). Each of these techniques provides a signal that is approximately proportional to the first or second differential of the phase shift of the electron wave that has passed through the sample.

In the Fresnel mode of Lorentz TEM, the intensity distribution at a defocus Δz below or above the specimen is imaged. In overfocus or underfocus images of a specimen that contains magnetic domain walls, the electron trajectories either converge or diverge out of focus at the position of each domain wall, as shown in Fig. 4(a). Magnetic contrast is then not visible in images that are recorded in focus. Since the electron deflection angle is small, large defocus values of several tens or hundreds of μ m are typically needed to record magnetic contrast out of focus. For a Bloch-type magnetic skyrmion, the presence of a rotating magnetic field (see below) results in an intensity maximum or minimum in a Fresnel defocus image, depending on its helicity and on the sign of the defocus [8]. Figures 4(b) and 4(c) show representative Fresnel defocus images of the same region of a $B20$ -type FeGe magnetic skyrmion lattice. The technique is straightforward to implement and provides a direct qualitative image that reveals the positions at which the in-plane magnetization in the sample changes abruptly. However, it is difficult to extract quantitative information from such images. Although quantitative information can be extracted from a series of defocused images by solving the "transport of intensity" equation, which is a phase retrieval method based on the relationship between the intensity derivative in the electron beam direction measured from defocused images and the lateral phase variation [9], the technique can suffer from artefacts resulting from a lack of knowledge of the boundary conditions in the phase or phase gradient at the edges of the field of view. The primary advantages of the Fresnel mode of Lorentz TEM for characterizing skyrmions are that it is simple to implement, provides a large field of view and allows skyrmion formation and movement to be followed in real time [10].

Since the first discovery of a skyrmion lattice (SkL) structure in Mn-Si [2], compounds based on the $B20$ -type crystal structure have been the most studied skyrmion-hosting materials. Most materials with this crystal structure are compounds of a transition metal and a group-14 element. The cubic crystal structure type belongs to the chiral space group $P2_13$ (No.198), which breaks the inversion symmetry and results in the possibility of non-superposable mirror atomic structures (enantiomers). Figure 5(a) shows a unit cell of $B20$ -type FeGe, which has a lattice constant $a = 4.689 \text{ \AA}$ and a magnetic transition temperature $T_C = 278.3 \text{ K}$. In such compounds, the

crystalline chirality affects their magnetism *via* spin-orbit coupling (SOC), resulting in the stabilization of magnetic structures that have a unique rotation sense, such as helical spin states and skyrmions. The spin arrangements in helical structures and Bloch-type skyrmions are shown schematically in Fig. 5(b). In the presence of inversion asymmetry and SOC, an additional exchange interaction, the DMI, contributes to the system energy and stabilizes a skyrmion lattice in the presence of a small perpendicular magnetic field. Some material parameters, such as the micromagnetic exchange constant \mathcal{A} , the DMI constant \mathcal{D} and the magnetization M_s , are related directly to experimentally measurable quantities. For example, the ratio of the micromagnetic and DMI constants determines the lowest period of an incommensurate spin spiral and the equilibrium period of the helical phase L_D , as well as the critical field corresponding to the saturation field of the system H_D , through the expressions

$$L_D = 4\pi \frac{\mathcal{A}}{\mathcal{D}}, \quad H_D = \frac{\mathcal{D}^2}{2M_s \mathcal{A}}. \quad (4)$$

The parameters L_D and H_D can be considered as fingerprints for each particular chiral magnet. TEM requires the examination of electron-transparent samples that are self-supporting and free of sample preparation artefacts. Bulk materials are now often prepared for TEM analysis in a dual-beam scanning electron microscope (SEM) equipped with a focused ion beam (FIB) system. The ability to image a sample in the SEM as it is milled with a focused Ga ion beam provides precise control over the sputtering and thinning processes. Figure 5(c) shows an SEM image of the topography of a FIB lamella prepared for TEM investigation. The lamella has a thickness of approximately 100 nm and is fixed to a Cu support grid, which is used to transfer it between the SEM and the TEM.

Since the transition temperature of FeGe is below room temperature, a liquid-nitrogen-cooled specimen holder needs to be used in the TEM to image the helical and skyrmion magnetic structure. A desired specimen temperature can be chosen by counter-heating the specimen during liquid nitrogen cooling. Below the transition temperature, the FeGe system is characterised by a helical magnetic structure in zero magnetic field, which transforms into a skyrmion lattice upon applying a perpendicular (out-of-plane) magnetic field to the sample. Figures 5(d) and 5(e) show Fresnel defocus images of typical helical and skyrmion spin structures recorded at a temperature of 240 K and 800 μm overfocus. The period of the helical phase L_D in FeGe is 70 nm. SkL formation takes place in an out-of-plane magnetic field of ~ 100 mT, while the system becomes saturated magnetically when the applied field reaches a few hundred mT.

2.2 Off-axis electron holography

The technique of holography was originally proposed by the Hungarian-British physicist Dennis Gabor (Gábor Dénes), in order to overcome the resolution problem in electron microscopy caused by spherical aberration [15, 16]. The method is based on the interference of a wave of primary interest with a (usually plane) reference wave. The resulting interference fringes are modulated locally in contrast and position by the amplitude and phase of the primary wave. Although there are several forms of electron holography, the most commonly used mode in the TEM is off-axis electron holography [17, 18, 19].

A conventional in-focus bright-field TEM image records variations in the intensity of the electrons that reach the detector and information contained in the phase of the electron wave is lost. Instead, phase information can be retrieved from an off-axis electron hologram, which is an interference pattern formed by the superposition of a complex specimen wave with a tilted plane

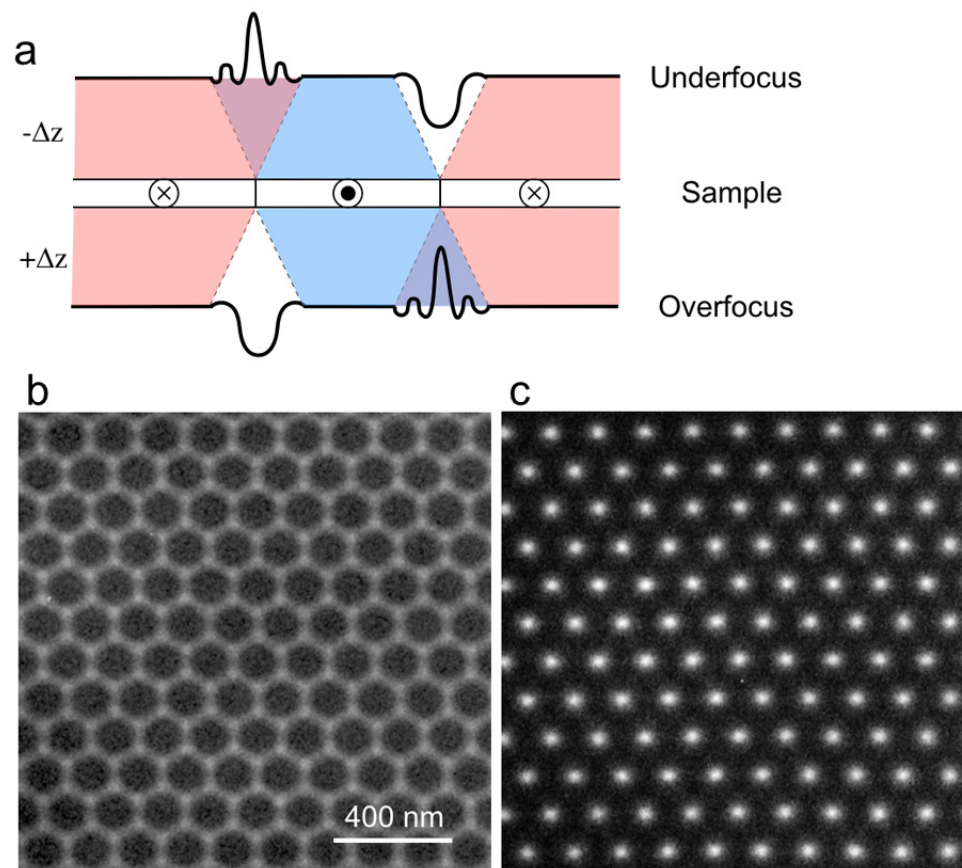


Fig. 4: Contrast formation in Fresnel defocus images. (a) Schematic diagram showing the deflection of electrons in a magnetic sample that contains anti-parallel domain walls, illustrating the formation of convergent and divergent contrast in overfocus and underfocus images. (b) Underfocus and (c) overfocus Fresnel images of a skyrmion lattice in a B20-type FeGe specimen recorded in the presence of a 100 mT out-of-plane magnetic field at a temperature of 200 K. The images were recorded at defocus values of ± 0.4 mm. The images in (b) and (c) are adapted from Ref. [14].

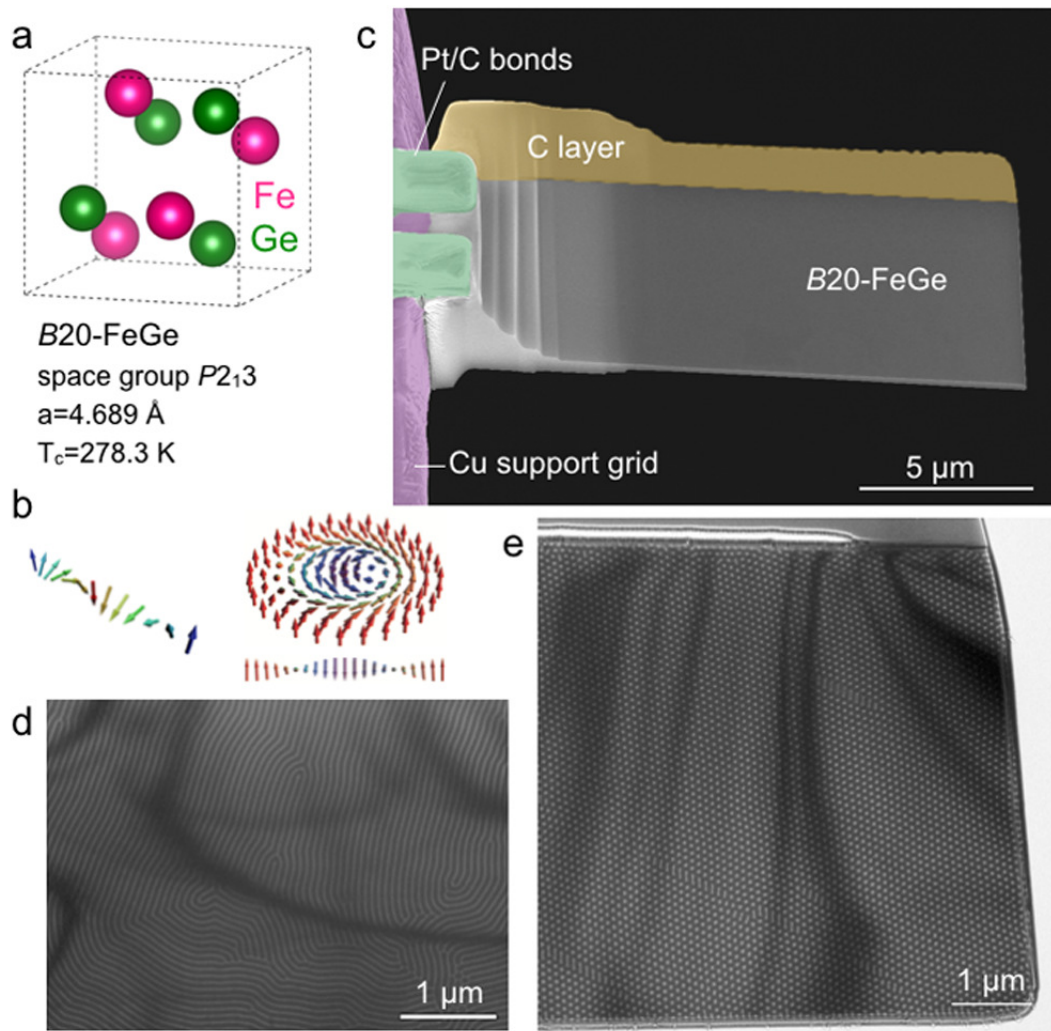


Fig. 5: B20-type FeGe. (a) Unit cell of B20-type FeGe, which has a magnetic transition temperature of 278.3 K. (b) Schematic representations of a helical spin structure and a Bloch-type skyrmion. (c) Secondary electron SEM image of a FIB-prepared lamella. The specimen thickness decreases gradually to 100 nm. (d, e) Fresnel defocus images of a helical spin structure and a skyrmion lattice, respectively, recorded at a temperature of 240 K and a defocus of 800 μm . Unpublished work.

reference wave. The intensity distribution in the recorded interference pattern can be written in the form

$$I(x, y) = A_{i1}^2 + A_{i2}^2 + 2A_{i1}A_{i2}\cos(\Delta\phi) , \quad (5)$$

where A_i is the amplitude of each wave and $\Delta\phi$ is the phase difference between them at each point across the field of view.

Figure 3 illustrates the fact that off-axis electron holography is based on the interference of an electron wave that has passed through a region of interest on the sample (the object wave) with another part of the same electron wave that has usually passed only through vacuum (the reference wave). An electron holographic interference pattern is generated by applying a positive voltage to an electrostatic biprism wire. The spacing of the interference fringes and the width of the “overlap region” are controlled by the biprism voltage and the microscope lens set-up. Practical off-axis electron holography requires the use of a highly coherent electron beam from a field emission gun electron source. The electron beam that is incident on the sample is often deliberately adjusted to be highly elliptical, with an aspect ratio that can exceed 100:1, in order to maximize the coherency of the electrons at the sample plane while maintaining a sufficiently short acquisition time. A stable electron microscope and sample environment and a balance between coherence, intensity and acquisition time are needed to maximize the contrast of the interference fringes and, therefore, to minimize noise in the final retrieved phase image. The electrostatic biprism is typically a sub- μm -diameter metal or metal-coated quartz wire. It is mounted in a conventional selected area aperture rod and positioned close to a conjugate image plane in the microscope, requiring a careful readjustment of the electron optics. In general, the application of a higher biprism voltage results in a larger overlap width, a finer interference fringe spacing s and a decrease in interference fringe contrast [11], which is defined according to the expression $C = (I_{max} - I_{min}) / (I_{max} + I_{min})$, where I_{max} and I_{min} are the maximum and minimum interference fringe intensities recorded in vacuum, as shown in Fig. 3. Although off-axis electron holograms have traditionally been recorded on negatives and analysed on laser benches, they are now almost always recorded digitally using either CCD cameras or modern direct electron detectors, which offer improved dynamic range and speed.

In a quantum mechanical description, an incident electron wave experiences a phase shift upon travelling through an electromagnetic potential that can be expressed (in one dimension) in the form

$$\phi(x) = \phi_E + \phi_M = C_E \int V(x, z) dz - \frac{2\pi e}{h} \int A_z(x, z) dz , \quad (6)$$

where the incident electron beam direction z is perpendicular to x , C_E is an interaction constant that takes a value of $6.53 \times 10^6 \text{ radV}^{-1}\text{m}^{-1}$ at an accelerating voltage of 300 kV, V is the electrostatic potential and A_z is the component of the magnetic vector potential along z . The magnetic vector potential \mathbf{A} is related to the magnetic flux density by the expression $\mathbf{B} = \nabla \times \mathbf{A}$. In the absence of long-range charge redistribution within and around the sample and electron-beam-induced specimen charging, V comprises primarily the mean inner potential (MIP) of the material V_0 , which depends on its composition, density and ionicity. Then, if the MIP does not vary within specimen thickness t , the electrostatic contribution to the phase shift can be simplified to $\phi_E = C_E V_0 t$.

The magnetic contribution to the phase shift resulting from an enclosed magnetic flux Φ_M (without the necessity for classical interaction with a B field) was predicted by Ehrenberg and Siday [12] and Aharonov and Bohm [13]. The effect was verified experimentally using electron holography by several groups, in excellent agreement with theory. The magnetic contribution

to the recorded phase shift between two arbitrary points in a phase image can be written in the form

$$\phi_M = -\frac{2\pi e}{h} \oint Adl \quad (7)$$

for a rectangular loop that is formed by two parallel electron trajectories crossing the sample and joined, at infinity, by segments perpendicular to their trajectories. With reference to Eq. 7, Stokes' law can be used to show that

$$\phi_M = -2\pi \frac{e}{h} \Phi_M(S) , \quad (8)$$

where $h/e = 4.135 \times 10^{-15} \text{ Tm}^2$ is a flux quantum (the magnetic flux that results in a phase difference of 2π) and S is the area of the loop that encloses the magnetic flux. A graphical representation of the projected in-plane magnetic flux distribution in the sample can be obtained by adding contours to the recorded magnetic contribution to the phase. It is usually essential to separate the MIP and magnetic contribution to the phase in order to obtain quantitative magnetic information about the sample. One of the possible approaches for achieving this separation is described below.

Figure 6 shows the sequence of experimental and data processing steps that is required to obtain a magnetic induction map of a *B20*-type FeGe skyrmion lattice. Off-axis electron holograms are first recorded from the sample and from a vacuum reference area using the same illumination conditions (Figs 6(a, b)). The inset in (a) shows a magnified region of interference fringes, which are slightly bent as a result of local variations in in-plane magnetic field across the field of view. In this case, the vacuum reference hologram was acquired from a region where there are no significant electrostatic or magnetic fields. The Fourier transform of the electron hologram of the sample (Fig. 6(c)) contains a centreband and two sidebands, as well as streaks that are associated with Fresnel fringes from the edges of the biprism wire. The local variation in intensity around the sidebands results from phase shifts introduced by the sample (and the microscope lenses).

Reconstruction of the holograms involves digitally selecting one of the sidebands using an aperture (Fig. 6(c)), followed by centering it in Fourier space and calculating its inverse Fourier transform. The phase of the resulting complex image $\phi = \arctan(i/r)$ is evaluated from the imaginary i and real r parts of the wavefunction, while the amplitude is obtained from the expression $A = \sqrt{r^2 + i^2}$. The difference between the object phase and the phase of the vacuum reference hologram (Fig. 6(d)) is initially evaluated modulo 2π and therefore contains phase discontinuities, which can be “unwrapped” using suitable algorithms (Fig. 6(e)).

In order to separate the magnetic contribution to the phase shift from the MIP contribution, phase images of the *B20*-type FeGe sample were recorded both at low temperature (Fig. 6(e)) and at room temperature (Fig. 6(f)). The two phase images were then aligned and subtracted from each other (on the assumption that the MIP is the same and that there are no changes in diffraction contrast or specimen charging between the two temperatures). Figure 6(g) shows the final magnetic contribution to the phase shift of the skyrmion lattice in *B20*-type FeGe. By generating contours and colours from the magnetic contribution to the phase, a magnetic induction map (Fig. 6(h)) is obtained.

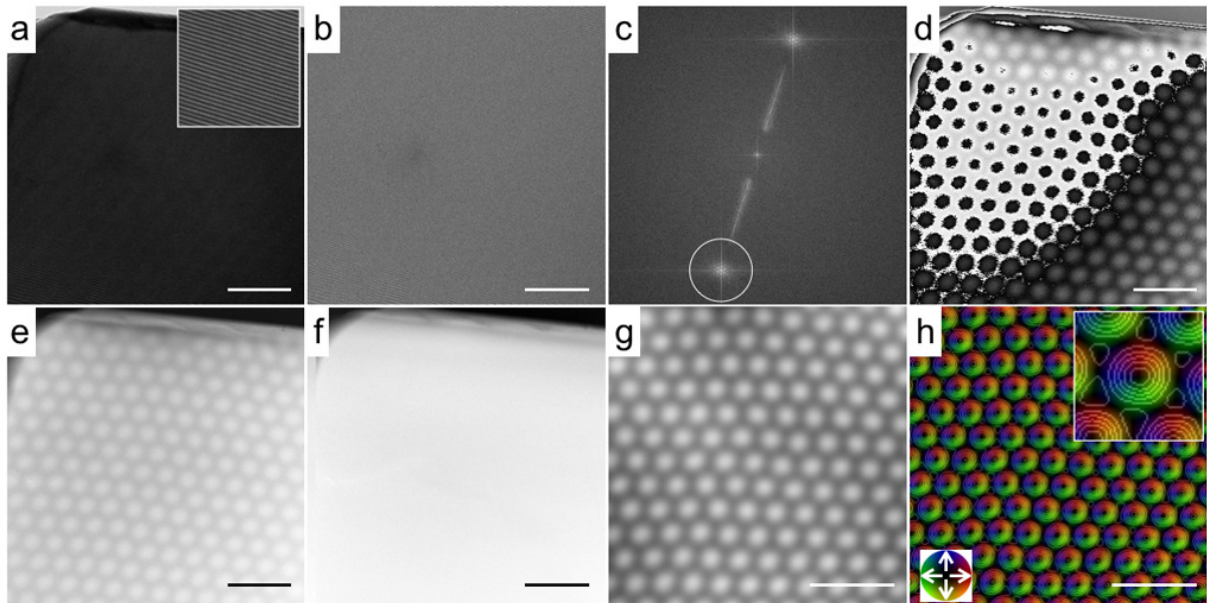


Fig. 6: Sequence of processing steps used to obtain quantitative magnetic induction maps of magnetic skyrmions in B20-type FeGe. (a, b) Off-axis electron holograms of sample and vacuum regions, respectively, with the sample at 200 K in the presence of a 100 mT out-of-plane magnetic field. The interference fringe spacing is approximately 2.4 nm. (c) Central part of the Fourier transform of the sample hologram, showing a centreband, two sidebands and streaks originating from the Fresnel fringes from the edges of the biprism wire. By selecting one of the sidebands, masking the region outside the marked circle, moving it to the origin of Fourier space and performing an inverse Fourier transform, the complex specimen wave function can be retrieved. (d, e) Wrapped and unwrapped phase images after subtracting the phase of the vacuum reference hologram. (f) Unwrapped phase image of paramagnetic FeGe recorded at room temperature. (g) Magnetic phase image obtained by subtracting the mean inner potential contribution to the phase shown in (f) from the phase image shown in (e). (h) Magnetic induction map generated from the magnetic phase image in (g), showing a clockwise rotation of the magnetic field in the skyrmions. An enlargement of part of the magnetic induction map and a colour wheel are shown as insets. The scale bar is 200 nm. The contour spacing in (h) is $2\pi/64 = 0.098$ radians. Unpublished work.

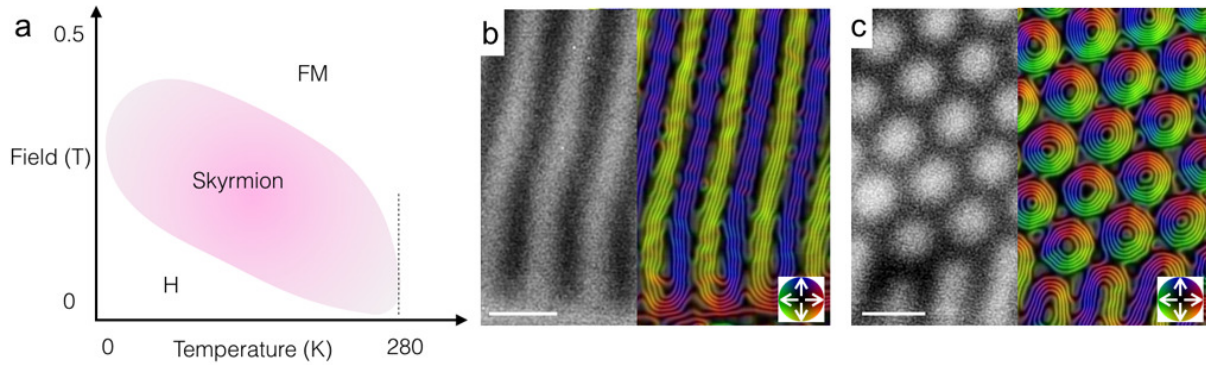


Fig. 7: (a) Schematic B - T phase diagram of the magnetic phases in $B20$ FeGe. The regions marked “H”, “Skyrmion” and “FM” denote a helical structure, a skyrmion lattice and a saturated ferromagnetic state, respectively. The critical temperature of the system is 278.3 K. (b) Magnetic phase shift and magnetic induction map of the helical structure recorded at 95 K in zero magnetic field. (c) Magnetic phase shift and magnetic induction map of a skyrmion lattice recorded at 95 K in the presence of a 100 mT out-of-plane magnetic field. In each magnetic induction map, the contour spacing is 0.098 radians and a colour wheel is inset. The scale bar in (b) and (c) is 80 nm. Unpublished work.

3 Quantitative measurements of skyrmions in $B20$ -type FeGe

Both the remanent magnetic state of a sample and its magnetic microstructure in an applied magnetic field can be characterized quantitatively with high spatial resolution using Lorentz microscopy and off-axis electron holography. Additional information can be obtained by applying external stimuli to the sample, such as electric field, light and temperature, *in situ* in the TEM. Here, the characterization of the magnetic states of Bloch-type skyrmions in thin films of $B20$ -type FeGe as a function of temperature and magnetic field is described. The skyrmions form a lattice in the presence of a small out-of-plane magnetic field, which can be applied to the sample by partially exciting the conventional microscope objective lens, as shown in Fig. 7. In this way, the magnitudes of local variations in the magnetic contribution to the phase shift across individual skyrmions recorded using off-axis electron holography can be studied quantitatively as a function of temperature and magnetic field, in order to create a detailed experimental phase diagram of magnetic states in $B20$ -FeGe thin films.

3.1 Temperature and magnetic field dependence

We begin by describing the examination of a FIB-prepared specimen below the critical temperature of FeGe using a liquid nitrogen cooling holder, while controlling the pre-calibrated magnetic field applied to the sample by changing the current of the microscope objective lens *in situ* in the TEM. Figure 8 shows the temperature and magnetic field dependence of a SkL in a $B20$ -FeGe thin film measured using off-axis electron holography. A perfect hexagonal SkL initially forms upon cooling the sample below the critical temperature in the presence of a small out-of-plane magnetic field (Fig. 8(a)). The average magnetic phase shift of an individual skyrmion was measured to be ~ 0.7 radians at 95 K for the present sample thickness. The analysis of magnetic induction maps recorded at higher temperature revealed that the hexagonal order remains, but the magnetic phase shift of each skyrmion is reduced, as shown in Figs 8(b),

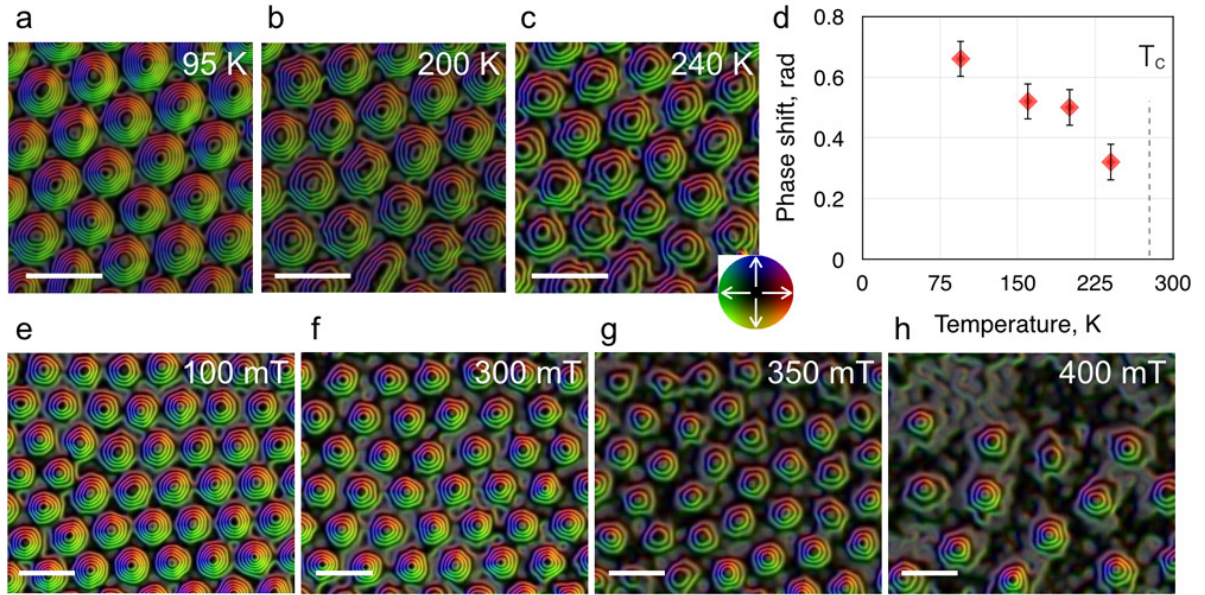


Fig. 8: Temperature and magnetic field dependence of skyrmions in B20-type FeGe. (a-c) Magnetic induction maps of a skyrmion lattice recorded in a 100 mT out-of-plane magnetic field at 95, 200 and 240 K, respectively. The magnetic induction maps were generated from magnetic phase images obtained using off-axis electron holography. (d) Phase shifts across skyrmions measured from magnetic phase images, plotted as a function of temperature. (e-h) Magnetic induction maps of a skyrmion lattice recorded at 200 K in out-of-plane magnetic fields of 100, 300, 350 and 400 mT, respectively. The contour spacing in each magnetic induction map is $2\pi/64 = 0.098$ radians. A colour wheel is shown alongside (c). Adapted from Ref. [14]

8(c) and 8(d). The magnitude of the measured phase shift decreases gradually as the temperature is increased to 280 K. These observations suggest that the critical temperature in a thin film of B20-FeGe is identical to the bulk value.

The magnetic field dependence of the skyrmion lattice was studied by applying out-of-plane magnetic fields \mathbf{B}_{ext} to the sample. Figures 8(e) and 8(h) show transformations of the skyrmion lattice as the magnetic field was increased to 400 mT at a constant temperature of 200 K. As the magnetic field was increased to 300 mT, the skyrmion lattice started to deviate from a hexagonal arrangement, becoming disordered at approximately 350 mT. A gradual decrease in skyrmion core diameter (not shown) was accompanied by an expansion of the lattice period. At 400 mT, the number of skyrmions decreased significantly. Between adjacent skyrmions, the sample then became fully saturated by the applied magnetic field. At 450 mT, no skyrmions remained and the sample was fully saturated magnetically parallel to the applied field direction. The measured magnetic phase shifts of individual skyrmions were observed to decrease with increasing applied field.

The detailed magnetic configurations of individual skyrmions in a SkL were analysed [20] using the symmetrized spin rotation distribution $\theta(\rho, \varphi)$, as shown in Fig. 9. Figure 9(a) shows a schematic illustration of the magnetic configuration of a single skyrmion in a SkL. The magnetic moment vectors \mathbf{m} at the core and edge are antiparallel and parallel to the direction of the applied magnetic field \mathbf{B}_{ext} , respectively. In the intermediate region, \mathbf{m} rotates from the core to the edge of the skyrmion in a rotational sense, which is right-handed in this case. The spin rotation angle θ is defined in Fig. 9(b). It is convenient to describe the magnetic structure as

a function of distance from the centre of a skyrmion, on the assumption that it can be treated as an almost axially symmetrical object. The detailed shapes of skyrmions determined from different phase images were compared by normalizing each radial phase profile $\phi(\rho)$ so that the differences $\Delta(\phi)$ between the peaks and dips were identical, as shown in Fig. 9(c) for different temperatures in an out-of-plane magnetic field of 100 mT. The consistency between the curves indicates that there is no significant dependence of skyrmion structure on temperature over the studied range of applied magnetic field. Figure 9(d) shows normalized profiles of θ plotted for different values of applied magnetic field at 200 K. The θ profiles are observed to vary significantly with applied magnetic field. By analysing the spin rotation angle θ , it can be seen that the value of ρ at which \mathbf{m} has an in-plane direction becomes smaller with increasing applied magnetic field (Fig. 9(d)). This behaviour can be understood in terms of an increasing magnetic component parallel to the applied field direction as a result of a gain in Zeeman energy. The experimental results were compared to micromagnetic simulations for an isotropic chiral magnet. Equilibrium skyrmion states were found by energy minimization of the continuum functional, which contains terms describing Heisenberg exchange, the DMI, the Zeeman energy and the demagnetizing field energy. Micromagnetic calculations revealed that the demagnetizing field significantly changes the \mathbf{B}_{ext} dependence of the skyrmion periodicity and magnetization. The energy terms describing both the demagnetizing field and the Zeeman energy are sensitive to the absolute value of the spontaneous magnetization, which is generally temperature dependent.

3.2 *In situ* magnetization switching of a skyrmion lattice

In the previous experiment, the external magnetic field \mathbf{B}_{ext} was applied to the sample using the weakly excited objective lens of the microscope. The direction of the applied magnetic field, as well as its magnitude, can be changed, allowing the switching mechanisms of skyrmions to be observed directly. Here, we show Fresnel defocus images and electron holographic phase images recorded as a function of the magnitude and direction of the applied magnetic field \mathbf{B}_{ext} .

Figure 10 shows a hysteresis curve for a switching process measured from the average magnetic phase shift recorded using off-axis electron holography. Corresponding Fresnel defocus images show directly that the starting state is a perfect hexagonal lattice of skyrmions in an applied out-of-plane magnetic field of +100 mT at 240 K. The direction of the magnetic field of each skyrmion core is usually antiparallel to the applied field direction. On decreasing the magnitude of the applied field, the skyrmion lattice is partially destroyed and a local helical structure develops. As the strength of the magnetic field is further changed in the opposite direction, the helical structure transforms into a skyrmion lattice at an applied magnetic field of 95 mT. The reverse process involves the same sequence of steps, with the skyrmion lattice transforming to a helical structure and then to the original skyrmion lattice. The results show that the switching process that occurs when the direction of the magnetic field is reversed involves a transition through a helical structure, before a skyrmion lattice forms with opposite magnetization relative to the starting configuration at a given substrate temperature. However, it should be noted that the response of skyrmions to the strength and direction of an external field can also depend strongly on both specimen temperature and specimen geometry.

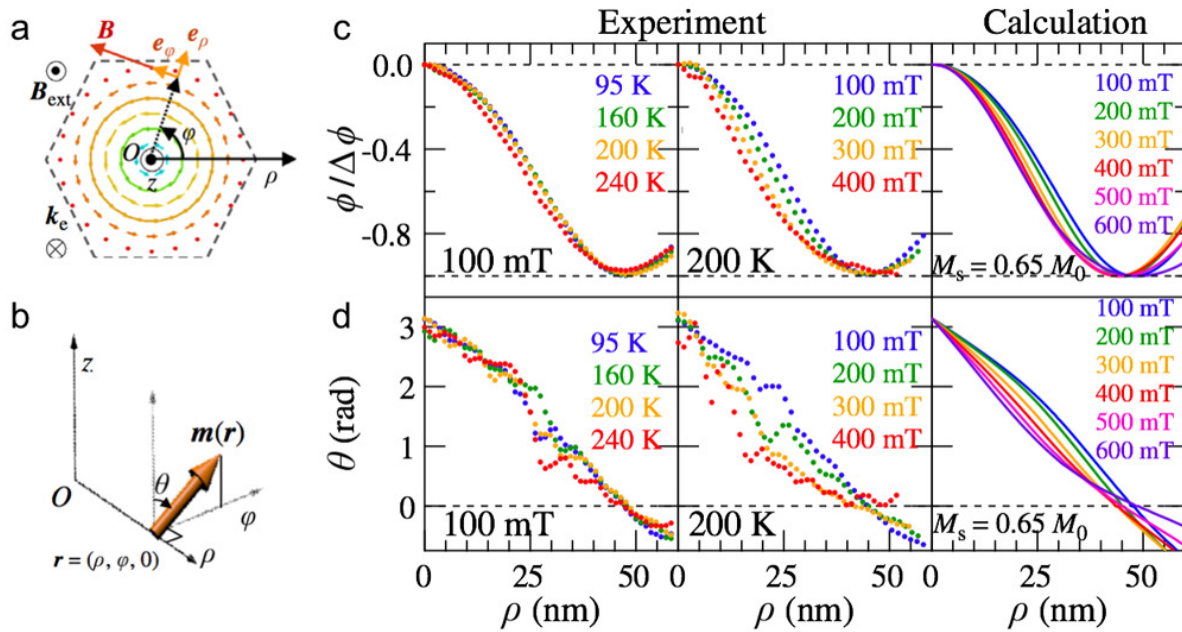


Fig. 9: Analysis of the temperature and magnetic field dependence of the internal skyrmion structure in a skyrmion lattice in B20-type FeGe. (a) Schematic diagram of the magnetic configuration of a skyrmion, shown alongside the definition of a cylindrical coordinate system (ρ, φ, z) . \mathbf{B}_{ext} and \mathbf{k}_e are the external magnetic field and the wave vector of the incident electron beam, respectively. (b) Definition of spin rotation angle θ . (c, d) Experimental measurements and theoretical calculations of the normalized phase distribution across a skyrmion at different temperatures and magnetic fields plotted as a function of distance ρ from its centre. Adapted from Ref. [20]

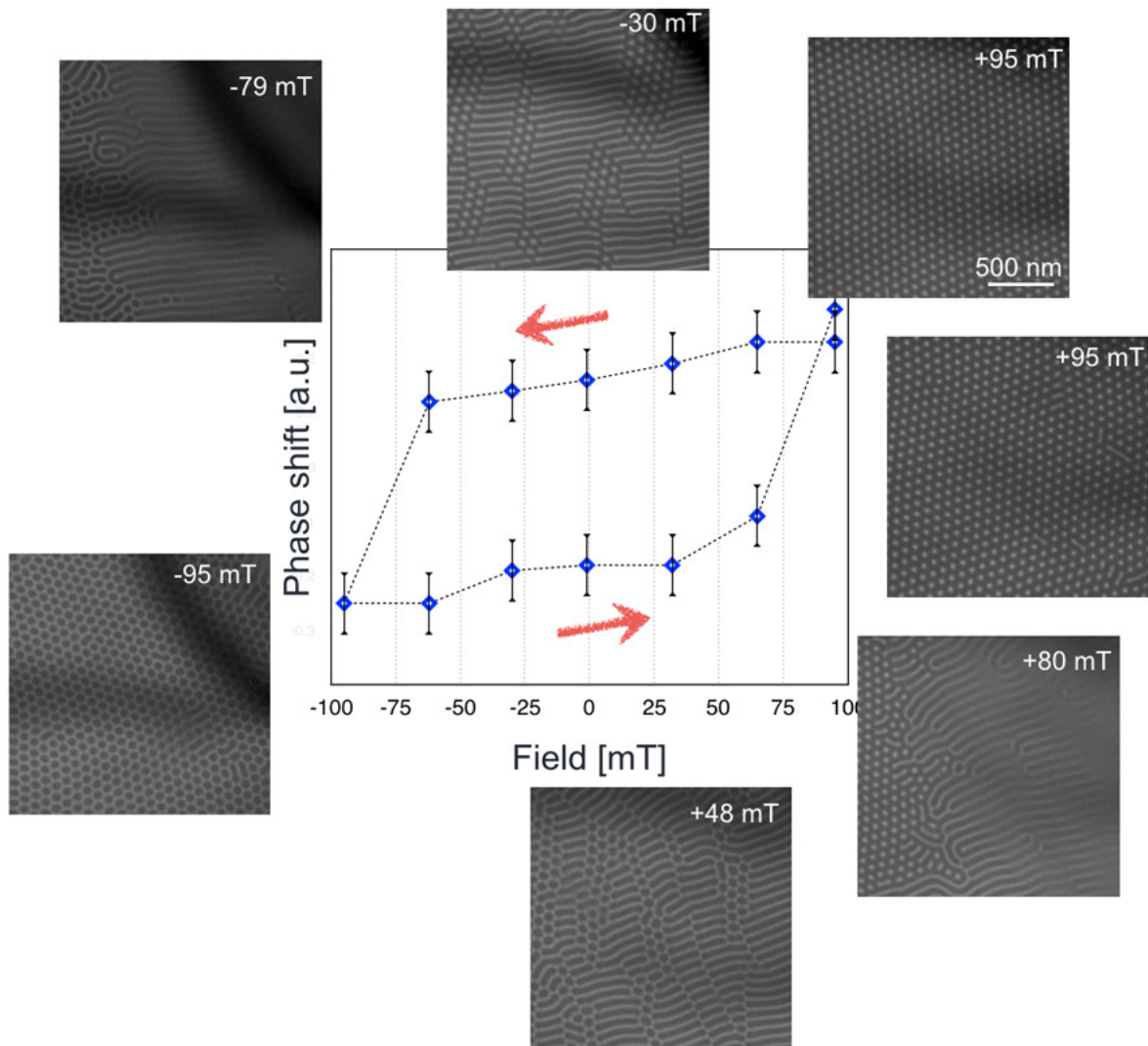


Fig. 10: Magnetization reversal process of a skyrmion lattice in B20 FeGe recorded at 240 K. The Fresnel defocus images shown in the figure were recorded $800 \mu\text{m}$ overfocus. The average phase shift values shown in the graph were measured from experimental magnetic phase images recorded using off-axis electron holography. The magnetic field was applied perpendicular to the sample plane. Unpublished work.

3.3 Skyrmions in confined geometries

In a thin film of a $B20$ -type chiral magnet, an external magnetic field can be used to stabilize a highly perfect hexagonal magnetic skyrmion lattice. Recently, several theoretical proposals have suggested that an isolated skyrmion can be created by using *e.g.*, a spin polarized electric current and that its motion can be driven by a current-induced torque [21]. Alternatively, the use of a confined specimen geometry is a promising approach for hosting either individual skyrmions or linear arrays of skyrmions, simply by impeding lattice formation in a geometry such as a narrow stripe. More details about skyrmion dynamics can be found in Chapter C9. The sample geometry can be controlled either by depositing a desired pattern of the magnetic material or by fabricating a specific sample geometry directly from the bulk material.

As discussed above, FIB preparation can be used to fabricate a thin section of bulk $B20$ FeGe, in order to study skyrmions. In the same way, FIB milling can be used to prepare a needle-shaped sample, whose diameter can be scaled according to the characteristic sizes of helical and skyrmion periodicities in the material. Figure 11(a) shows an SEM image of a FIB-prepared FeGe needle. A Pt/C layer, which can be seen at the end of the needle, was used to protect it from ion beam damage during FIB milling. The needle diameter increases linearly from ~ 100 nm to above a μm . At reduced temperature and in the presence of an applied magnetic field, skyrmions in the needle form a chain-like geometry, which transforms into a zig-zag skyrmion structure as the needle becomes wider, as shown in a Fresnel defocus image in Fig. 11(b). Preliminary analysis of the shapes of individual skyrmions in the needle reveals elliptical distortions prior the formation of the zig-zag arrangement. Figures 11(c) and 11(d) show quantitative magnetic induction maps of the needle recorded using off-axis electron holography. The skyrmion state is accompanied by a magnetized region that runs along the edges of the needle in antiparallel directions. Theoretical analysis suggests that such an edge spin configuration can be regarded as a type of surface state in a chiral magnet. The fact that it preserves the chirality of the spin texture around the edge of the sample has been anticipated to play a key role in current-induced skyrmion motion in magnetic nanostripes. Figures 11(c) and 11(d) show that the skyrmions have symmetrical shapes in the zig-zag structure and at the end of the single chain of skyrmions. Between these two regions, the skyrmions adopt a sequence of stretched elliptical morphologies with increasing needle diameter. It is remarkable that the ratio of longitudinal to transverse ellipticity of the most highly stretched skyrmions is approximately 2, *i.e.*, that the skyrmions can increase their size to twice their normal diameter.

On the basis of both detailed experimental characterization of wedge-shaped samples and theoretical calculations, a temperature *vs* applied magnetic field phase diagram [22] was created for $B20$ -FeGe skyrmions formed in confined geometries, as shown in Fig. 12. At a low value of applied magnetic field, a distorted helical spin structure is present. This spin structure transforms into a pure edge twist, a single skyrmion chain or a zig-zag skyrmion chain in the presence of an applied magnetic field of approximately 75 mT, depending on the width of the sample. The limiting width of a sample that can support a single skyrmion chain is between 79 and 160 nm. Within this range, skyrmions exhibit longitudinal and transverse elliptical distortions, respectively. In the phase diagram, W_y^c corresponds to the critical width for the formation of ideally circular skyrmions. Depending on the applied magnetic field, either a single skyrmion chain or a zig-zag skyrmion chain forms in samples that have widths of above 160 nm. The appearance of a zig-zag chain reflects the tendency of interacting skyrmions to condense into a hexagonal lattice when they are densely packed. The optimal width of a sample that contains a single chain of undistorted skyrmions is estimated to be 110 nm for $B20$ FeGe.

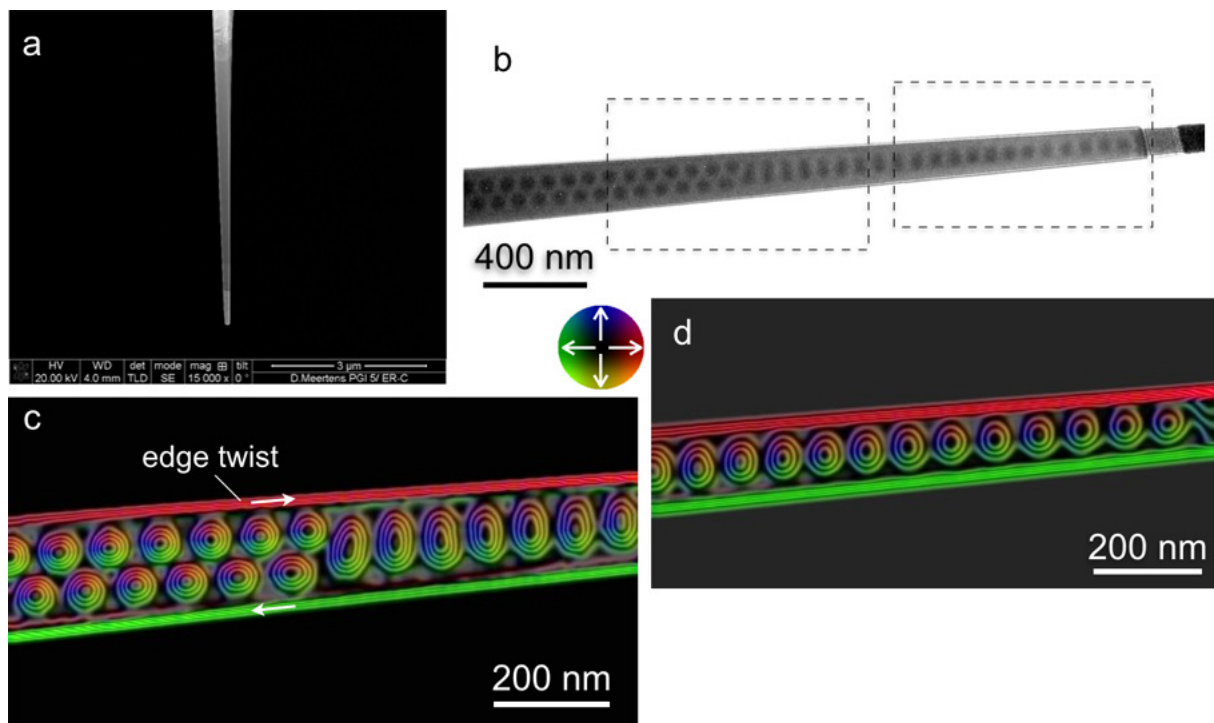


Fig. 11: Magnetic skyrmions in B20-FeGe in confined geometry. (a) Secondary electron SEM image of a FIB-prepared needle-shaped specimen of FeGe. (b) Fresnel defocus image recorded in an externally applied out-of-plane magnetic field of 100 mT at a sample temperature of 200 K, showing a single line of skyrmions that rearranges into a zig-zag structure where the needle is wider. (c, d) Magnetic induction maps of the marked regions in (b) recorded using off-axis electron holography. The contour spacing is 0.098 radians. Unpublished work.

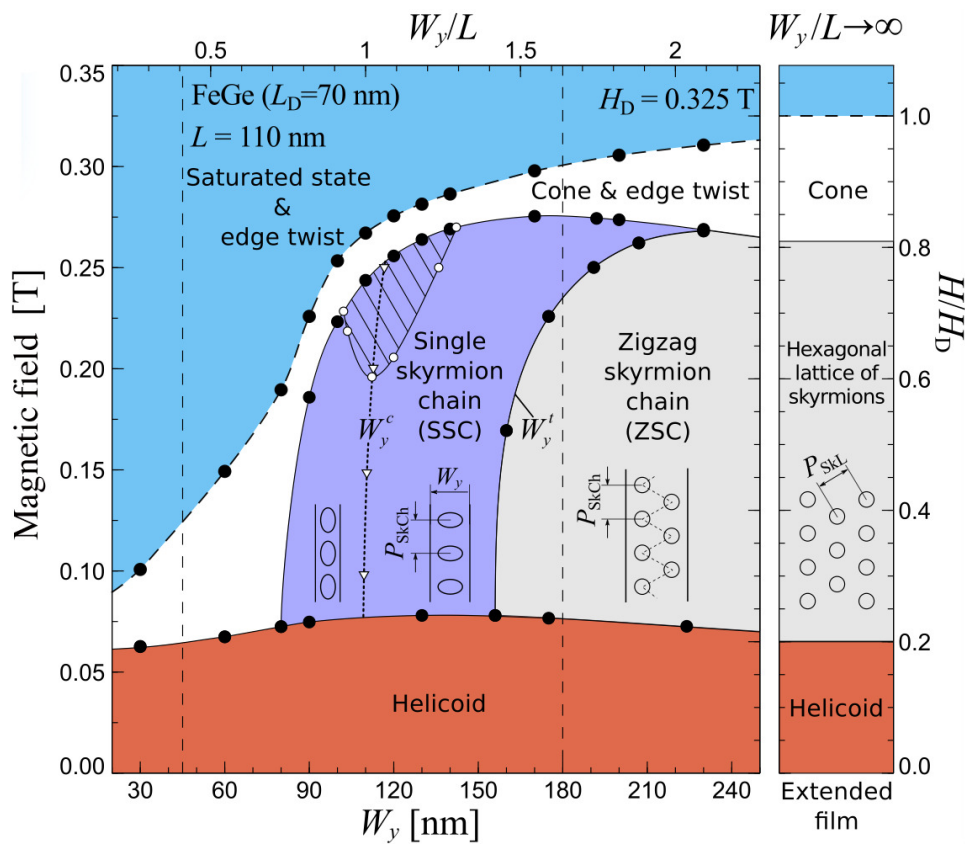


Fig. 12: Phase diagram of skyrmions in a nanostripe of B20-FeGe determined from both experimental results and simulations. W_y is the width of the sample and L is its thickness. Adapted from Ref. [22]

3.4 Magnetization and hexagonal distortion of skyrmions

In a ferromagnetic material, the magnetic flux density \mathbf{B} is defined by the well-known relation $\mathbf{B} = \mu_0(\mathbf{H} + \mathbf{M})$, where μ_0 is the permeability in vacuum, \mathbf{H} is the auxiliary or demagnetizing field and \mathbf{M} is the magnetization. As outlined above, off-axis electron holography is sensitive to the projected in-plane magnetic induction \mathbf{B} within and around a sample. Recently, a method has been developed to allow the magnetization \mathbf{M} in a sample to be determined from one or more magnetic phase images recorded using off-axis electron holography [23]. In this approach, a forward model is implemented in an iterative model-based algorithm for reconstructing the projected in-plane or three-dimensional magnetization distribution in the sample. It makes use of known analytical solutions for the magnetic contribution to the phase shift of geometrical objects and uses precomputed convolution kernels to determine their contribution to the phase shift.

This iterative approach can be used to perform high spatial resolution mapping of the projected in-plane magnetization (as opposed to the projected in-plane magnetic flux density) of individual skyrmions, in order to analyse their distortions when they are in a lattice. In this context, it is of particular interest to establish the flexibility of the skyrmion spin structure in a hexagonal lattice.

As discussed above, a skyrmion lattice forms upon applying a low magnitude of out-of-plane magnetic field. The lattice transforms into a disordered arrangement of individual skyrmions at higher values of applied magnetic field (Fig. 8). Single skyrmions were selected from experimental phase images and their projected in-plane magnetization was determined using the iterative model-based algorithm described above, as shown in Fig. 13. Whereas preliminary analysis of the experimental phase images does not suggest strong deformation of the skyrmions when they are in a lattice, the projected in-plane magnetization shown in Figs 13(b) and 13(c) reveals a hexagonal distortion, with a displacement of the hexagon edges of approximately 4 nm from a circular shape. In addition, a shear in the skyrmion shape results from imperfections of the skyrmion lattice, as a result of a dislocation in the skyrmion arrangement (Fig. 8(e)). At higher applied magnetic fields, the distance between individual skyrmions and their neighbours increases and their shapes approach perfect circles, as shown in Figs 13(e) and 13(f).

4 Summary

In this chapter, we have illustrated how highly resolved imaging using Lorentz TEM and off-axis electron holography can be combined with theoretical modelling to provide new insight into the internal structure and behaviour of Bloch-type skyrmions in the $B20$ -type chiral magnet FeGe. We examine skyrmions in different sample geometries as a function of temperature and applied out-of-plane magnetic field and show that off-axis electron holography, in particular, can be used to provide quantitative magnetic induction maps that can be interpreted in terms of projected in-plane magnetization by applying numerical inversion algorithms. The real space observation of magnetic skyrmions in a TEM using Fresnel imaging and off-axis electron holography is indispensable for understanding their structures and magnetic properties.

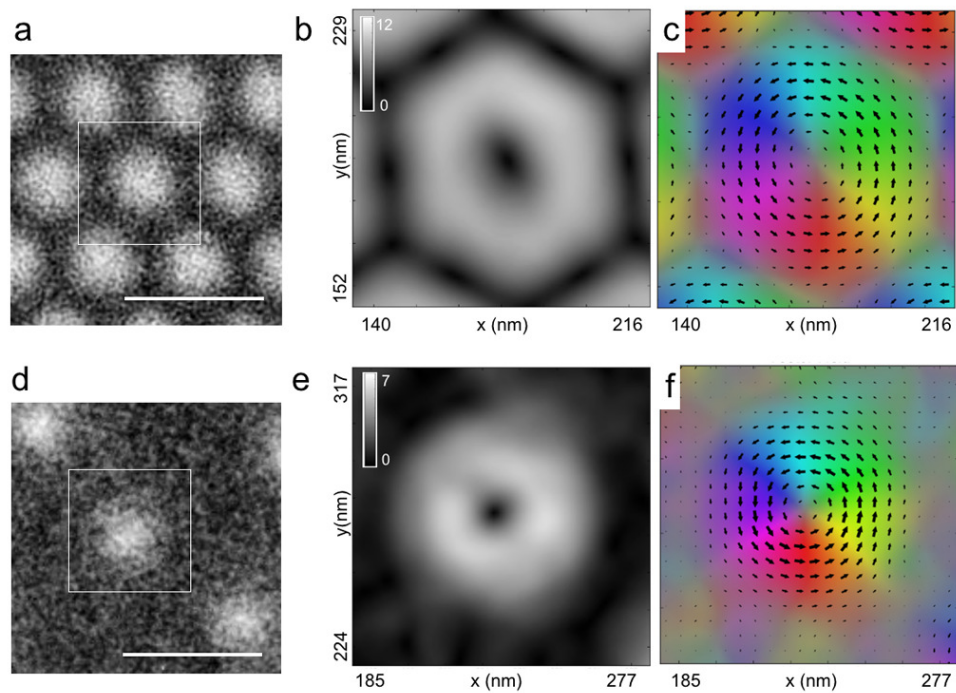


Fig. 13: Magnetization mapping of individual skyrmions. (a, d) Magnetic phase images of a skyrmion lattice and individual skyrmions recorded at 200 K in the presence of out-of-plane magnetic fields of 100 and 400 mT, respectively. The scale bar is 100 nm. (b, e) Corresponding maps of projected in-plane magnetization obtained from the phase images using a model-based iterative reconstruction algorithm. (c, f) Vector field maps of the projected in-plane magnetization. Unpublished work.

Acknowledgments

The authors are grateful to K. Shibata, Y. Tokura, Z.-A. Li, J. Caron, H. Du, F. Zheng, N. Kiselev, S. Blügel, D. Meertens, M. Farle and other colleagues for their contributions to this work and for ongoing collaborations. The research leading to these results has received funding from the European Research Council under the European Union's Seventh Framework Programme (FP7/2007-2013)/ ERC grant agreement number 320832.

References

- [1] A.N. Bogdanov, D.A. Yablonskii, *Thermodynamically stable vortices in magnetically ordered crystals. The mixed state of magnets*. Sov. Phys. -ETP **68**, 101 (1989).
- [2] S. Mühlbauer, B. Binz, F. Jonietz, C. Pfleiderer, A. Rosch, A. Neubauer, R. Georgii, P. Böni, *Skyrmion lattice in a chiral magnet*. Science **323**, 915 (2009).
- [3] X.Z. Yu, Y. Onose, N. Kanazawa, J.H. Park, J.H. Han, Y. Matsui, N. Nagaosa, Y. Tokura Y, *Real-space observation of a two- dimensional skyrmion crystal*. Nature **465**, 901 (2010).
- [4] X.Z. Yu, N. Kanazawa, W.Z. Zhang, T. Nagai, T. Hara, K. Kimoto, Y. Matsui, Y. Onose, Y. Tokura, *Skyrmion flow near room temperature in an ultralow current density*. Nat. Commun. **3**, 988 (2012).
- [5] P.J. Grundy, *Magnetic bubbles and their observation in the electron microscope*. Contemp. Phys. **18**, 47 (1977).
- [6] D.B. Williams, C.B. Carter, *Transmission Electron Microscopy: A Textbook for Materials Science*. (Springer, 2009).
- [7] C.L. Jia, S.B. Mi, J. Barthel, D.W. Wang, R.E. Dunin-Borkowski, K.W. Urban, A. Thust. *Determination of the 3D shape of a nanoscale crystal with atomic resolution from a single image*. Nat. Mat. **13**, 1044 (2014).
- [8] K. Shibata, X.Z Yu, D. Morikawa, N. Kanazawa, K. Kimoto, S. Ishiwata, Y. Matsui, Y. Tokura, *Towards control of the size and helicity of skyrmions in helimagnetic alloys by spin-orbit coupling*. Nat. Nanotech. **8**, 723 (2013).
- [9] C. Phatak, A.K. Petford-Long, and M. De Graef, *Recent advances in Lorentz microscopy*. Current Opinion in Solid State and Materials Science **20**, 107 (2016).
- [10] J. Rajeswari, P. Huang, G.F. Mancini, Y. Murooka, T. Latychevskaya, D. McGrouther, M. Cantoni, E. Baldini, J.S. White, A. Magrez, T. Giamarchi, H.M. Ronnow, F. Carbone, *Filming the formation and fluctuation of skyrmion domains by cryo-Lorentz transmission electron microscopy*. PNAS **112**, 14212 (2015).
- [11] T. Kasama, R.E. Dunin-Borkowski, M. Beleggia, *Electron holography of magnetic materials*. Chapter 3 in “Holography - Different Fields of Application”, pp. 53-80, edited by F.A. Monroy Ramírez (InTech, 2011).
- [12] W. Ehrenberg, R.E. Siday, *The refractive index in electron optics and the principles of dynamics*. Proc. Phys. Soc. Lond. B **62**, 8 (1921).
- [13] Y. Aharonov, D. Bohm, *Significance of electromagnetic potentials in quantum theory*. Phys. Rev. **115**, 485 (1959).
- [14] A. Kovács, Z-A. Li, K. Shibata, R.E. Dunin-Borkowski, *Lorentz microscopy and off-axis electron holography of magnetic skyrmions in FeGe*. Resolution and Discovery **1**, 2 (2016).
- [15] D. Gabor, *A new microscopic principle*. Nature **161**, 563 (1948).

- [16] D. Gabor, *Microscopy of reconstructed wave-fronts*. Proc. Roy. Soc. **197**, 454 (1949).
- [17] H. Lichte, M. Lehmann, *Electron holography - basics and applications*. Rep. Prog. Phys. **71**, 016102 (2008).
- [18] M.R. McCartney, D.J. Smith, *Electron holography: Phase imaging with nanometer resolution*. Ann. Rev. Mat. Res. **37**, 729 (2007).
- [19] R.E. Dunin-Borkowski, T. Kasama, M. Beleggia and G. Pozzi, *Lorentz microscopy and electron holography of magnetic materials*. Chapter 6 in the “Handbook of Nanoscopy”, pp. 221-252, edited by G. van Tendeloo, D. van Dyck and S.J. Pennycook (Wiley-VCH, 2012).
- [20] K. Shibata, A. Kovács, N.S. Kiselev, N. Kanazawa, R.E. Dunin-Borkowski, Y. Tokura, *Temperature and magnetic field dependence of the internal and lattice structures of skyrmions by off-axis electron holography*. accepted for publication in Phys. Rev. Lett. (2017).
- [21] J. Sampaio, V. Cros, S. Rohart, A. Thiaville, A. Fert, *Nucleation, stability and current-induced motion of isolated magnetic skyrmions in nanostructures*. Nature Nanotechnology **8**, 839 (2013).
- [22] C. Jin, Z-A. Li, A. Kovács, J. Caron, F. Zheng, F.N. Rybakov, N.S. Kiselev, H. Du, S. Blügel, M. Tian, Y. Zhang, M. Farle, R.E. Dunin-Borkowski, *Control of morphology and formation of geometrically confined magnetic skyrmions*. Submitted for publication.
- [23] J. Caron, J. Ungermann, M. Riese, R.E. Dunin-Borkowski, *Model-based reconstruction of magnetization from electron-optical phase images: I. A fast and accurate forward model*. Submitted for publication.